

CrRhAs: a member of a large family of metallic kagome antiferromagnets

Y. N. Huang

Department of Physics, Zhejiang University of Science and Technology, Hangzhou 310023, People's Republic of China

Harald O. Jeschke

Research Institute for Interdisciplinary Science, Okayama University, Okayama 700-8530, Japan

Igor I. Mazin*

Department of Physics & Astronomy, George Mason University, Fairfax, VA 22030, USA and Quantum Science and Engineering Center, George Mason University, Fairfax, VA 22030, USA.

(Dated: November 10, 2022)

Kagome lattice materials are an important platform for highly frustrated magnetism as well as for a plethora of phenomena resulting from flat bands, Dirac cones and van Hove singularities in their electronic structures. We study the little known metallic magnet CrRhAs, which belongs to a vast family of materials that include $3d$, $4f$ and $5f$ magnetic elements, as well as numerous nonmagnetic metals and insulators. Using noncollinear spin density functional calculations (mostly spin spirals), we extract a model magnetic Hamiltonian for CrRhAs. While it is dominated by an antiferromagnetic second nearest neighbor coupling in the kagome plane, the metallic nature of the compound leads to numerous nonzero longer range couplings and to important ring exchange terms. We analyze this Hamiltonian and find unusual ground states which are dominated by nearly isolated antiferromagnetic triangles that adopt 120° order either with positive or with negative vector chirality. We discuss the connection to the few known experimental facts about CrRhAs. Finally, we give a brief survey of other interesting magnetic members of this family of kagome compounds.

I. INTRODUCTION

Due to strong geometric frustration, antiferromagnetism on a kagome lattice is expected to yield novel properties such as classical or quantum spin liquids [1–4]. A good example with well-localized spin-1/2 copper magnetic moments forming a kagome lattice is herbertsmithite ($\text{ZnCu}_3(\text{OH})_6\text{Cl}_2$) which is drawing a lot of interest since it was first synthesized in 2005 [5]. It has long been discussed as a quantum spin liquid candidate [6] but some kind of structural disorder plays a significant role [7]. Other examples of kagome antiferromagnets which are proximate to or actually realize quantum spin liquids are kapellasite ($\text{ZnCu}_3(\text{OH})_6\text{Cl}_2$) [8, 9], Y-kapellasite ($\text{Y}_3\text{Cu}_9(\text{OH})_{19}\text{Cl}_8$) [10, 11] and Zn-barlowite ($\text{ZnCu}_3(\text{OH})_6\text{FBr}$) [12, 13].

More recently, metallic kagome materials with or without magnetism have been studied intensively. A typical example is the intermetallic T_mX_n kagome series ($T = \text{Mn, Fe, Co}$; $X = \text{Sn, Ge}$; $m:n = 3:1, 3:2, 1:1$) with different kagome plane stackings [14]. Much effort has been put into studying their topological properties (Dirac Fermions and flat bands) [14–16]. Related kagome metals, such as YMn_6Sn_6 , exhibit a nontrivial topological Hall effect [17–19], while another kagome metal, AV_3Sb_5 ($A = \text{K, Na, Cs}$) demonstrates a series of intriguing orders, including superconductivity [20–23]. Importantly, kagome planes in these systems are not magnetically frustrated, but they retain interesting electronic

properties due to the special features of the kagome dispersion, Dirac point, van Hove singularities and flat band. Kagome metals with antiferromagnetic frustration have been little studied so far [24, 25].

Ideal kagome lattices are not uncommon, but relatively rare. An important point in this regard is that most unique properties of kagome magnets do not, actually, require an ideal kagome *geometry*, but rather an ideal kagome *connectivity*. In this respect, there is no difference at the nearest neighbor level between a perfect kagome lattice and the one twisted by triangle rotations, as shown in Fig. 1. In this paper, we discuss a large family of compounds with the chemical formula XYZ and space group $P\bar{6}2m$ (no. 189). Typically, they include two metal layers, X and Y with ligands Z integrated into the two layers at a ratio 1:2. Thus, the structure can be understood as a stacking of Y_3Z_2 at $z = 0$ and of X_3Z at $z = 0.5$. Due to two 6-fold rotoinversion axes, the metal planes can be described as twisted kagome, where ligands sit in high-symmetry positions inside the metal planes. One metal sublattice, as discussed below, is only moderately deformed from the ideal kagome, while the other, incorporating two ligand atoms per unit cell, has metals fitted into trimers. The former subsystem is often magnetic, the latter usually not.

The elemental base for this crystallographic family, known by its prototype ZrNiAl , where $X = \text{Zr}$, $Y = \text{Al}$, and $Z = \text{Ni}$, is large, and metallic layers can be formed by transition metals, lanthanides, actinides, alkaline earths, etc. Many of the compounds are magnetic, when X forms the magnetic sublattice, and the resulting frustration is identical to the ideal kagome model. A known but little

* imazin2@gmu.edu

studied representative of this family is CrRhAs [26–29]. We have chosen it as an example to perform an extensive study of its in-plane and out-of-plane magnetic interactions, using density functional theory (DFT) calculations. We use the energies of spin spirals to extract the important parameters of a Heisenberg plus ring exchange Hamiltonian. We find that the second inplane exchange interaction clearly dominates over the first, leading to a spiral magnetic ground state.

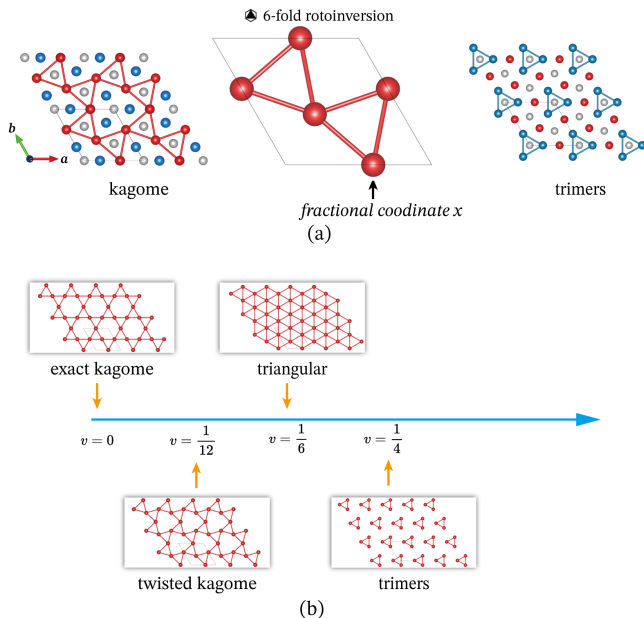


FIG. 1. (a) Two 6-fold rotoinversion axes in the unit cell of the $P\bar{6}2m$ XYZ compound (center). x is the fractional coordinate of the X atom indicated by an arrow. The left panel shows red atoms forming a kagome sublattice which is twisted by triangle rotations. The right panel shows blue atoms forming triangles. (b) The type of sublattice is uniquely determined by $v = x - 1/2$. When $v = 0$, the sublattice is exact kagome; When $|v| < 1/6$, it is a twisted kagome; when $|v| > 1/6$ it is trimers. The VESTA visualization program [30] was used to generate this figure.

II. XYZ COMPOUNDS WITH $P\bar{6}2m$ STRUCTURE

In XYZ with $P\bar{6}2m$ space group, both X and Y sublattices are characterized by one distortion parameter $v = x - \frac{1}{2}$, where x is the coordinate of the $3g$ ($3f$) Wyckoff position. The $3g$ and $3f$ positions differ only in the z coordinate, $1/2$ and 0 , respectively. The Z ions occupy two sublattices, $1b$ in the $3g$ plane, and $2c$ in the $3f$ plane. Increasing the absolute value of the distortion parameter $|v|$ makes the equilateral X triangles grow and rotate in the X_3Z plane. This takes the X sublattice from an ideal kagome lattice at $v = 0$ via a kagome lattice with rotated triangles and deformed hexagons for $0 < |v| < \frac{1}{6}$

and a perfect triangular lattice at $|v| = \frac{1}{6}$ to trimers for $|v| > \frac{1}{6}$. At increasing $|v|$, the triangular lattice of Z at the $1b$ position is enclosed by ever smaller X triangles. The v parameter has the same effect in the Y_3Z_2 plane with the difference that here, the Z in the $2c$ position form a honeycomb lattice. Thus, the connectivity in the two metal sublattices, X and Y, is different, which dramatically affects their magnetic properties. The compact triangles in the Y_3Z_2 plane tend to have considerable covalent bonding, and no, or little magnetism. The X ions, in contrast, form only a moderately twisted kagome lattice (minimizing the Coulomb interaction with the ligand in the center), and are likely to have magnetism which can be frustrated in case of antiferromagnetic interactions.

We have inspected the $P\bar{6}2m$ XYZ compounds on the materials project website [31] and organized some potentially magnetic ones into convenient tables, shown in Ref. [32], Tables S1 to S3. We found a number of XYZ compounds with significant magnetism, where magnetic kagome atoms can be Ce, Cr, Eu, Fe, Gd, Mn, Np, Pu, or U.

III. CrRhAs

We used a projector augmented wave basis as implemented in the Vienna ab initio simulation package (VASP) [33–35] to perform non-collinear magnetic calculations – when needed, with individual constraints. We use all electron calculations with the full potential local orbital (FPLO) basis [36] to plot band structure and Fermi surface. The generalized gradient approximation (GGA) in the Perdew-Burke-Ernzerhof variant (PBE) [37] was used as the exchange-correlation potential.

We base our calculations on the crystal structure of CrRhAs determined by Deyris *et al.* [38] (ICSD 43919) with $a = b = 6.384(1)$ Å and $c = 3.718(1)$ Å. The internal atomic positions of CrRhAs were relaxed in VASP while keeping lattice parameters fixed. The optimized structural parameters are shown in Table I, and will be used from now on.

TABLE I. GGA optimized fractional coordinates of CrRhAs.

Atom	Wyckoff	x	y	z
Cr	$3g$	0.6017	0	0.5
Rh	$3f$	0.2641	0	0
As1	$1b$	0	0	0.5
As2	$2c$	1/3	2/3	0

IV. MAGNETIC PATTERN ANALYSIS

In the following, we will infer magnetic couplings between Cr atoms based on energies of different magnetic

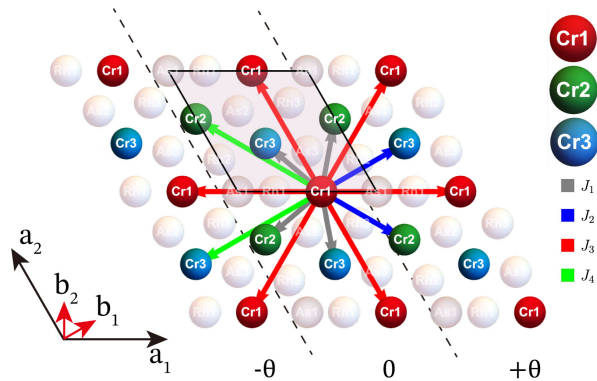


FIG. 2. 1st to 4th in-plane nearest neighbors in the Cr kagome sublattice in CrRhAs, indicated by arrows of different colors. The dashed lines cut the lattice into stripes corresponding to different spiral angles. Red, blue and green atoms are Cr1, Cr2, Cr3 respectively.

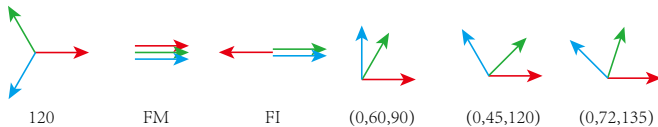


FIG. 3. 6 spin configurations within a unit cell that considered in spin spiral calculations. Red, Green, Blue arrows indicates moment directions of Cr1, Cr2, Cr3

patterns on the Cr sublattices. In Fig. 2, we define the three sublattices Cr1, Cr2, Cr3 of the kagome lattice. Arrows of different colors indicate the 1st to 4th in-plane nearest neighbor Cr atoms to a reference Cr1 atom. Each arrow associated with a Heisenberg term $J_n \mathbf{s}_i \cdot \mathbf{s}_j$ where J_n means n th in-plane nearest Heisenberg coupling and $\mathbf{s}_{i=1,2,3}$ means normalized spin operators for Cr1, Cr2, Cr3. The polar angles of moments are assumed to be $\phi(1), \phi(2), \phi(3)$ for Cr1, Cr2, and Cr3, respectively.

We will discuss spin spirals propagating along different directions and with 6 cases of spin configurations within a unit cell defined as 120, FM, FI, (0,60,90), (0,45,120), (0,72,135) as shown in Fig. 3. The $\phi(1), \phi(2), \phi(3)$ for each case are listed in Table. II. Besides, we also discuss periodic magnetic patterns with varying angle α as defined in Fig. 4

The total energy of a magnetic pattern on Cr sublattices can be written as

TABLE II. $\phi(1), \phi(2), \phi(3)$ (in degrees) for the six different spin spirals

spin configuration	$\phi(1)$	$\phi(2)$	$\phi(3)$
120	0	120	240
FM	0	0	0
FI	180	0	0
(0,60,90)	0	60	90
(0,45,120)	0	45	120
(0,72,135)	0	72	135

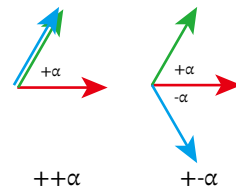


FIG. 4. Spin configuration of noncollinear $++\alpha$ and $+-\alpha$. Red, green and blue vector are spin moments of Cr1, Cr2 and Cr3 sublattice respectively.

tices can be written as

$$H = E_0 + H_{\text{Heisenberg}} + H_{\text{ring}} \quad (1)$$

where $H_{\text{Heisenberg}}$ is defined as

$$H_{\text{Heisenberg}} = \sum_{i < j} J_{ij} \mathbf{s}_i \cdot \mathbf{s}_j \quad (2)$$

Here, the $\mathbf{s}_i = \frac{1}{S} \mathbf{S}_i$ are magnetic moment vectors normalized to 1. We write the exchanges in the kagome plane as $J_{ij} = J_1, J_2, \dots$ where $1, 2, \dots$ correspond to increasing bond length (i.e. coordination shell). Exchange between the kagome layer and the next layer above and below are $J_{ij} = J'_0, J'_1, J'_2, \dots$, again sorted by distance (J'_0 is straight up or down). $J_{ij} = J''_0, J''_1, J''_2, \dots$ are bonds connecting second layers, and so on.

H_{ring} is the ring exchange on Cr triangle defined as

$$H_{\text{ring}} = L_1 \sum_{\Delta_1} \mathbf{s}_i \cdot \mathbf{s}_j + L_2 \sum_{\Delta_2} \mathbf{s}_i \cdot \mathbf{s}_j \quad (3)$$

where

$$\sum_{\Delta_1 \text{ or } \Delta_2} = (\mathbf{s}_1 \cdot \mathbf{s}_2)(\mathbf{s}_2 \cdot \mathbf{s}_3) + (\mathbf{s}_1 \cdot \mathbf{s}_3)(\mathbf{s}_3 \cdot \mathbf{s}_2) + (\mathbf{s}_2 \cdot \mathbf{s}_1)(\mathbf{s}_1 \cdot \mathbf{s}_3) \quad (4)$$

Here, sum over Δ_1 or Δ_2 means $\mathbf{s}_{i=1,2,3}$ are three moments of Cr1, Cr2, Cr3 that form 1st or 2nd nearest Cr triangle. L_1 and L_2 are corresponding triangle ring exchange strengths.

With the above definitions, we can rewrite the total energy in Eq.5 as

$$E = E_0 + L_1 D_1 + L_2 D_2 + \left(\sum_i J_i C_i + \sum_i J'_i C'_i + \dots \right) \quad (5)$$

where C_i, C'_i, D_1, D_2 are summations of terms like $\mathbf{s}_i \cdot \mathbf{s}_j$ and $(\mathbf{s}_i \cdot \mathbf{s}_j)(\mathbf{s}_j \cdot \mathbf{s}_k)$ that depend on magnetic patterns.

A. Spin spiral configurations

Spin spirals were modeled using the generalized Bloch theorem [39], as implemented in VASP. We calculated various spin spiral configurations for CrRhAs in order to get consistent information about the magnetic coupling

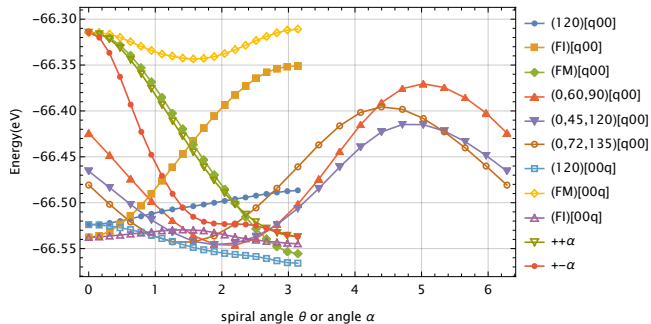


FIG. 5. Energy curves of 6 $(q, 0, 0)$ spirals, 3 $(0, 0, q)$ spirals, $++\alpha$ and $+-\alpha$.

between Cr atoms in CrRhAs. A spin spiral is determined by a propagation vector \mathbf{q} within the first Brillouin zone of the reciprocal space lattice. We mainly considered $(q_x, 0, 0)$ and $(0, 0, q_z)$ spirals.

The $(q_x, 0, 0)$ spirals are propagating along reciprocal \mathbf{b}_1 direction which is shown in Fig. 2. To understand the connectivity in these spirals, we can divide the lattice into stripes (dashed lines in Fig. 2) running along the unit cell vector \mathbf{a}_2 which is perpendicular to \mathbf{b}_1 . From one stripe to the next, all moments are rotated by the angle $\theta_x = \mathbf{q} \cdot \mathbf{a}_1$. There is an additional freedom of choosing Cr moment directions $\phi(1), \phi(2), \phi(3)$ within the unit cell, which generates different spin configurations. We considered six types of $(q_x, 0, 0)$ spin spirals, labeled as $(120)[q00]$, $(\text{FM})[q00]$, $(\text{FI})[q00]$, $(0, 60, 90)[q00]$, $(0, 45, 120)[q00]$, $(0, 72, 135)[q00]$ and corresponding $(0, 0, q_z)$ spirals labeled by replacing $[q00]$ with $[00q]$. For $(0, 0, q_z)$, a spiral propagates along the \mathbf{a}_3 direction, which is much simpler. All moments in a horizontal plane have the same spiral angle, and in the next plane along the \mathbf{a}_3 direction, they rotate by $\theta_z = \mathbf{q} \cdot \mathbf{a}_3$. Explaining the energetics of such spirals requires out of plane exchange couplings.

Simple, if tedious, calculation renders a Heisenberg Hamiltonian which is a linear form in J_s and L , with the coefficients C_i and D for general $(q_x, 0, q_z)$ spin spiral, as shown in Ref. [32] (Table. S5). For each spiral of the 120, FI, and FM cases, we performed spiral total energy calculations from spiral angle 0 to π , because their energy is symmetric with respect to spiral angle π up to J_4 . For the other cases, $(0, 60, 90)$, $(0, 45, 120)$, $(0, 72, 135)$, we calculated the full spiral angle range 0 to 2π .

B. Noncollinear periodic calculations

We also consider simple periodic cases where only the three Cr sublattices have different noncollinear spin directions, as shown in Fig. 4, and where we vary the angle α . Taking the spin direction of Cr1 as reference, in the $++\alpha$ case the spin directions of Cr2 and Cr3 are rotated by the same angle $+\alpha$, while in the $+-\alpha$ case, the spin

direction of Cr2 and Cr3 are rotated by $+\alpha$ and $-\alpha$, respectively. The energy versus α curves and their fittings to different orders of cosine are shown in Ref. [32] (Fig. S2).

If the magnetic interaction is dominated by Heisenberg type contributions, we would expect that a simple $\cos(\alpha)$ will fit the $++\alpha$ curve well. As we can see from Fig. S2 (see Ref. [32]), the fit is indeed not bad with single $\cos(\alpha)$, but after adding $\cos(2\alpha)$ it becomes much better. For the $+-\alpha$ case, we would expect $\cos(\alpha)$ plus $\cos(2\alpha)$ will fit well. However, it turns out that fitting to the order of $\cos(2\alpha)$ still has a large discrepancy with the calculated energies, and by adding a $\cos(3\alpha)$ term, two curves immediately snap together. So it is clear that explaining the $+-\alpha$ curve needs the $\cos(3\alpha)$ term.

One probable explanation is that there is ring exchange between three Cr atoms. For the spins $\mathbf{s}_1, \mathbf{s}_2, \mathbf{s}_3$ of $\text{Cr}_{i=1,2,3}$, a ring exchange interaction is proportional to $(\mathbf{s}_1 \cdot \mathbf{s}_2)(\mathbf{s}_2 \cdot \mathbf{s}_3) + (\mathbf{s}_1 \cdot \mathbf{s}_3)(\mathbf{s}_3 \cdot \mathbf{s}_2) + (\mathbf{s}_2 \cdot \mathbf{s}_1)(\mathbf{s}_1 \cdot \mathbf{s}_3)$. In the $+-\alpha$ case, this will introduce $\cos(\alpha)\cos(2\alpha)$ and $\cos(\alpha)^2$ terms, and $\cos(\alpha)\cos(2\alpha)$ is equivalent to $\frac{1}{2}(\cos(3\alpha) + \cos(\alpha))$, so that $\cos(3\alpha)$ emerges as soon as we consider ring exchange. For the $++\alpha$ case, the ring exchange term introduces additional $\cos(\alpha)^2$ contributions which also improves the fit.

C. Fitting all energy curves

Energies of six $(q_x, 0, 0)$ spirals, three $(0, 0, q_z)$ spirals, $++\alpha$ and $+-\alpha$ are shown in Fig. 5. Note that we have intentionally shifted the curves of $++\alpha$ and $+-\alpha$ up to align with $(\text{FM})[q00]$ and $(\text{FM})[00q]$ at $\theta = 0$, because due to the internal realization of VASP, energies of noncollinear and spiral calculations have a constant shift. From Fig. 5 The 120[00q] with $\theta = \pi$ has the lowest energy. This means that the interlayer coupling is AFM, and moments on Cr atoms on the same triangle tend to form the 120 degrees with each other.

Now we have 9 spiral curves plus 2 noncollinear curves with variable angle as shown in Fig. 5, which can be fit to Eq. 5, using Table S5 (see Ref. [32]). It appears that only a subset of J_s are linearly independent; furthermore, some longer-range couplings, while they can formally be extracted by the fit, come out very small and improve the fit only marginally. A choice of $E_0, J_1, J_2, J_3, J_4, J'_0, J'_1, J''_0, J''_1, L$ as a physically meaningful Hamiltonian gives good overall fits as shown in Fig. 6.

From this fitting result, we found that J_2 is the dominant exchange interaction. It is an antiferromagnetic coupling, and interestingly it is 10 times larger than the the second largest ferromagnetic exchange interaction J_1 . What is more, J_3, J_4 are also of the same order of magnitude as J_1 . The nearest and next nearest interlayer coupling is antiferromagnetic. Thus, we find a Heisenberg Hamiltonian with clearly dominating antiferromagnetic interactions, in agreement with the fact that experimen-

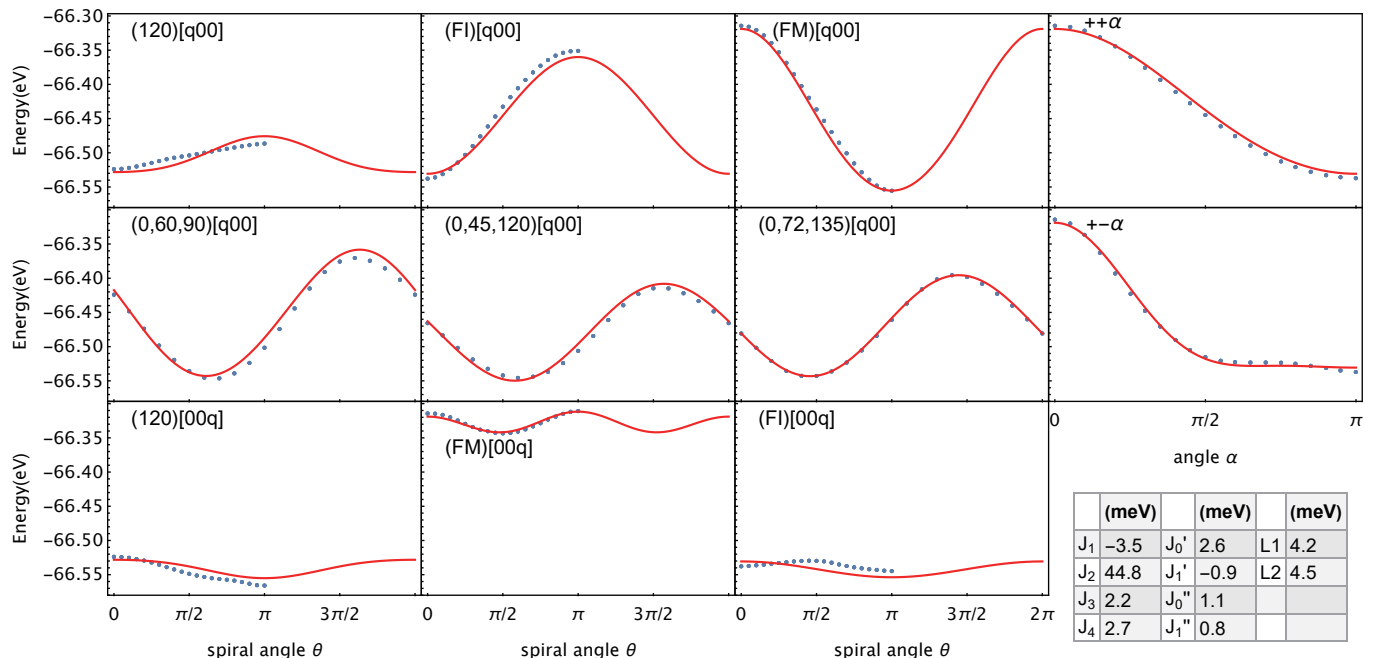


FIG. 6. Least square fit of six $(q_x, 0, 0)$ spirals, three $(0, 0, q_z)$ spirals, $++\alpha$ and $-\alpha$ to the Heisenberg Hamiltonian including four in-plane neighbors, two neighbors in the first and second interplanar interactions, and the nearest neighbor ring exchange, as discussed in the text. Blue symbols are calculated DFT energies. Red curves are the least squares fit with the parameters shown on the right.

tally, CrRhAs was found to order antiferromagnetically with a Neel temperature of $T_N = 165$ K [26]. Considering the hierarchy of exchange couplings, we expect the J_2 triangles to order in a 120 degree state. The second largest ferromagnetic J_1 couplings cannot be exactly satisfied because of J_1 - J_2 - J_1 triangles, and they already introduce some frustration. The smaller in-plane couplings J_3 and J_4 also contribute to frustration. Interestingly, even though the interlayer distances of CrRhAs are small, interlayer exchange is much smaller than in-plane exchange, and the material is magnetically rather two-dimensional.

Furthermore, the ring exchange term is indispensable for good fits of the DFT energies and is substantial at 12% of the dominant exchange interaction. Note that we can directly compare Heisenberg and ring exchange terms as we are using unit moments. As shown in Ref. [32], Fig. S3, without ring exchange, there are discrepancies between fitted and original data curves as large as 20 meV for $(120)[q00]$ and $(120)[00q]$ at $\theta = 0$, and similarly for $+\alpha$.

V. DISCUSSION OF THE EMERGING HAMILTONIAN

The Hamiltonian derived in the previous section is quite unusual. First, it is dominated by the large AF 2nd nearest-neighbor interaction (blue bonds). These

bonds form isolated triangles, all oriented in the same way. Each triangle, obviously, orders in a 120° fashion, and is formed by the three different Cr, Cr1, Cr2 and Cr3. Let us first for simplicity assume an XY model, so all spins lie in the ab plane (Fig. 8). There are two different ways to produce this order, illustrated in Fig. 7, differing by the sign of their vector chirality $\mathbf{W} = \mathbf{M}_1 \times \mathbf{M}_2 + \mathbf{M}_2 \times \mathbf{M}_3 + \mathbf{M}_3 \times \mathbf{M}_1$ on the dominant J_2 triangles. We use positive or negative vector chirality to distinguish between the two states (see Fig.7). Toroidal moment $\mathbf{T} = \sum_{i=1}^3 \mathbf{r}_i \times \mathbf{M}_i$ is usually nonzero for the state with positive vector chirality while it is always zero for the state with negative vector chirality. After one or the other types is selected, each blue triangle is fully determined by one of its spins (let's say, by the Cr1 spin). Then the lattice of the blue triangles is equivalent to a triangular lattice shown in red.

Let us now determine the effective Hamiltonian for this lattice: consider two blue triangles shifted along a . The Cr1 on the left is connected to Cr2' and Cr3' on the right, where "'" means the atoms from the right triangle. The corresponding contribution to energy is $J_1 \mathbf{S}_1 \cdot (\mathbf{S}_2' + \mathbf{S}_3') = -J_1 \mathbf{S}_1 \cdot \mathbf{S}_1'$. This, the FM n.n. interaction gives rise to an AF interaction for this green bond, which needs to be added to the, also AF, J_3 .

Let us now evaluate the interaction along b . By the same token, the coupling between the corresponding Cr2' atoms is also $J_{\text{eff}} = J_3 - J_1$. Since Cr2's are just the Cr1's in the same black triangle rotated by $2\pi/3$, it is the same

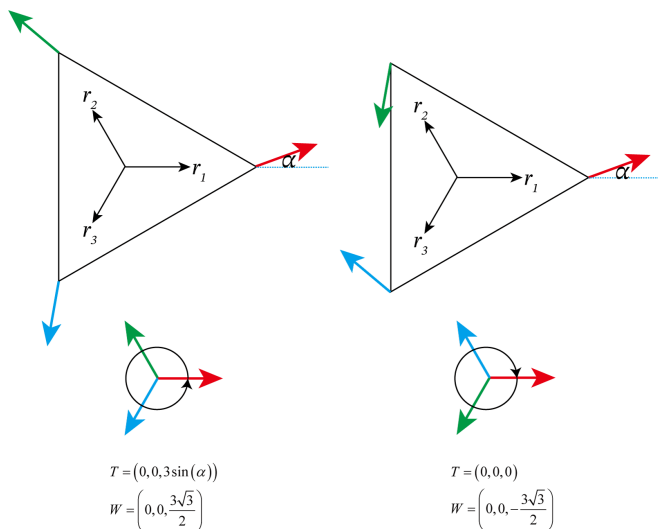


FIG. 7. Two topologically different 120° magnetic patterns on a triangle. Red, green and blue vector are spin moments of Cr1, Cr2 and Cr3 respectively. Note that the left pattern has an α dependent, usually nonzero toroidal moment $T = 3 \sin \alpha$ (assuming the black vectors r_i and magnetic moments have unit lengths), which can be continuously varied from 3 to -3 by rotating the spin space with respect to the coordinate space, while the right pattern has always $T = 0$, and that is not affected by the spin-space rotation. The left pattern has positive, the right negative vector chirality.

as adding J_{eff} along b for the Cr1 atoms (note that in principle we could rotate spins in the opposite directions when shifting along b compared to shifting along a , but that would have been energetically unfavorable).

Thus, we get a unique ground state, where the spins on the blue sublattice, which are of three different colors, form a 120° -lattice, and each color within itself also forms 120° -lattices. Next, let us look at the black triangles. Their centers are denoted by green and orange balls. They form a perfect honeycomb lattice, but it partitions (as the honeycomb lattice is bipartite) into two (triangular again) subsets (green and orange), one sporting FM triangles and the other 120° -triangles. Note that in terms of the *toroidal* moments it is reversed: the former subset has zero toroidal moments, while the latter non-zero ones. Note that the J_4 interaction, comparable with J_3 (but considerably smaller than $J_{\text{eff}} = J_3 - J_1$) is also satisfied as well as it is possible for a triangular lattice, *i.e.*, with 120° angles.

If we now select the other pattern with a positive vector chirality on the dominant J_2 (blue) triangles, we end up with an alternative structure, strictly degenerate with the first one (Fig. 8, bottom).

To summarize, the effective model can be mapped onto a triangular lattice where each site is characterized by a Heisenberg-spin variable (let us call it Σ , which shows the spin direction of the selected corner (Cr1, in this case), and another unit-length axial vector, Ω , showing

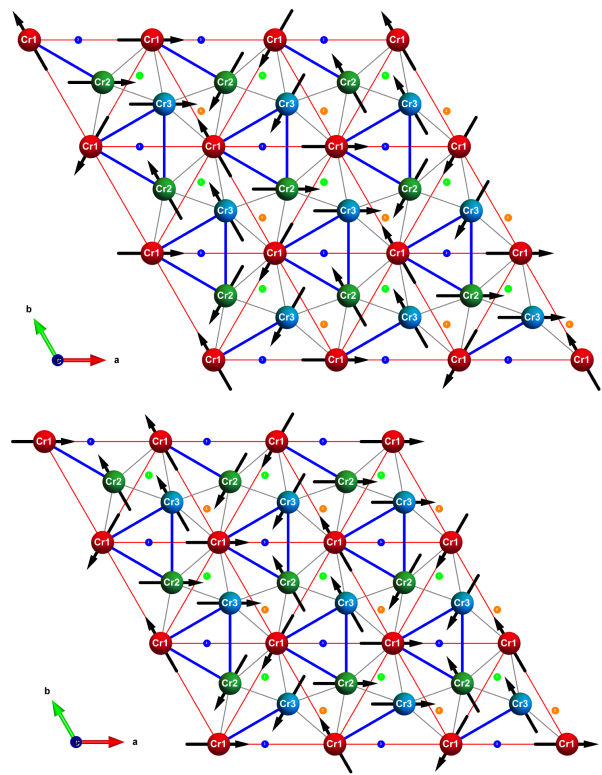


FIG. 8. Two possible 2D ground state of the reduced magnetic Hamiltonian including J_1 to J_4 interactions (note that the ground state is highly degenerate). The blue bonds indicate the strongest exchange coupling (AF) in the system (J_2), which generates 120° trimers, the grey bonds the nearest neighbor triangles, and the red one effective inter-trimer AF interaction, numerically equivalent to $J_3 - J_1$. Note that while in the ground state the blue trimers are ordered in a 120° fashion, and the red bonds network also assumes a 120° order, the two orders, in this model, are not correlated and may have different ordering planes and toroidal moments. The blue balls indicate centers of the blue trimers, the green and orange ones centers of the n.n. triangles. The top diagram corresponds to an order with negative vector chirality on the blue triangles, the bottom one to one with positive vector chirality.

the sense of the rotation in a given blue triangle (*i.e.*, rotations from Cr1 to Cr2 to Cr3 by $2\pi/3$ proceed around the axis Ω , and the sense of the rotation is given by the sign of Ω). The interaction between the effective spins Σ is also Heisenberg, AF, and much smaller than the interactions inside a trimer, and leads to a standard triangular Heisenberg order, which can also be characterized by a Heisenberg spin variable, \mathbf{S}_0 , which can be selected as the value Σ_0 at the origin, and another unit-length rotation vector, ω . At the end, the entire long-range magnetic order can be described by one Heisenberg spin Σ_0 and two axial rotational vectors Ω and ω . This is to be contrasted with the less-degenerate standard triangular lattice, which can be uniquely described by the origin spin and one rotational vector.

TABLE III. Toroidicity and chirality in the spin configuration with negative vector chirality on the dominant J_2 triangles, as discussed in the main text. For the purpose of this table, the two ordering planes are assumed parallel, $\Omega \parallel \omega$, so that the scalar chirality is always zero.

label	triangles	connectivity	effective coupling	net moment	toroidicity	vector chirality ($\parallel z$)
a	nearest neighbors	honeycomb	J_1	3	0	0
	sublattice 1			0	$[-3,3], \langle \dots \rangle = 0$	$3\sqrt{3}/2$
b	2nd neighbors	trimers	J_2	0	0	$-3\sqrt{3}/2$
c	centers of the “b” triangles ¹	triangular	$J_3 - J_1$	0	$[-3,3], \langle \dots \rangle = 0$	$\langle \dots \rangle = 0$
d	4th neighbors	trimers	J_4	0	0	$-3\sqrt{3}/2$

TABLE IV. Same as Table III, for the spin configuration with positive vector chirality on the dominant J_2 triangle.

label	triangles	connectivity	effective coupling	net moment	toroidicity	vector chirality ($\parallel z$)
a	nearest neighbors	honeycomb	J_1	3	0	0
	sublattice 1			0	0	$-3\sqrt{3}/2$
b	2nd neighbors	trimers	J_2	0	$[-3,3], \langle \dots \rangle = 0$	$3\sqrt{3}/2$
c	centers of the “b” triangles ¹	triangular	$J_3 - J_1$	0	$[-3,3], \langle \dots \rangle = 0$	$\langle \dots \rangle = 0$
d	4th neighbors	trimers	J_4	0	$[-3,3], \langle \dots \rangle = 0$	$3\sqrt{3}/2$

¹ equivalent to the 3rd neighbor triangles

Consideration of the second type of ordering, the one with positive vector chirality on the J_2 triangles, proceeds along the same lines. The results are summarized in Tables III and IV. The main difference is that in the former case half of the nearest neighbor triangles have non-zero toroidicity, which however averages to zero, while in the latter the same is true for the second-neighbor trimers.

Adding the ring exchange which we found to be sizeable does not alter this ground state. Indeed, it is easy to show that if an AF coupling on a triangle $J > 7L/2$ the ground state is not altered by adding the ring exchange. Finally, interaction along the c axis is strongly frustrated, with comparable J'_0 , J'_1 and J''_1 , which can lead, generally speaking, to spiral states propagating in this direction (given the higher coordination number for the last two).

While these two states have been discussed above in terms of supercells, one can notice that they also form spin spirals of a sort. Namely, the first one can be described, using our notations, as the $(120, 0, 0)[4\pi/3, 4\pi/3, 0]$ spiral, and the second as the $(0, 120, 120)[2\pi/3, 2\pi/3, 0]$ one. Note that in this Hamiltonian, the two spirals are degenerate, and have not been included in our previous calculations and fitting. Thus, these two states are true predictions and can be explicitly verified. Indeed, we found that, as predicted by the model Hamiltonian, they are (a) degenerate within computational accuracy and (b) 25.6 meV below the lowest-energy state found in the original calculations (namely, the standard 120° structure alternating antiferromagnetically between the planes.)

The last observation relates to the situation when the ordering planes are not parallel, $\Omega \not\parallel \omega$, a finite

local scalar chirality can be acquired, leading, for instance, to a topological Hall effect. This opens the door to a fluctuation-induced topological Hall effect at finite temperature[17]; however, further analysis is outside the scope of this paper.

VI. COMPARISON WITH EXPERIMENT

Experimental information on this material is, basically, limited to four papers from T. Kaneko and co-authors [26–29]. It has been established that CrRhAs experiences an antiferromagnetic transition, with the Néel temperature reported at $T_N = 165$ K [26–28] or 172 K [29]. The antiferromagnetic order has not been established. Interestingly, the magnetic susceptibility measured in an interval between T_N and room temperature is distinctly non-Curie-Weiss (CW). In the first publication, Ref. [26], it was fitted to the CW law, $\chi = C/(T - \Theta) + const$, but with a background of 1.47×10^{-3} emu/mole, which, if interpreted as Pauli susceptibility, corresponds to 45 states/eV·formula, or to an *ad hoc* formula $\chi = C'/(T - \Theta')^\gamma$, with $C' = 4.8 \times 10^{-3}$ emu K/mole, $\Theta' = 20$ K and $\gamma = 0.16$. In a later paper, Ref. [27], the same formula was used with $\chi = C'/(T - \Theta')^\gamma$, with $C' = 3.2 \times 10^{-2}$ emu K/mole, $\Theta' = -16$ K and $\gamma = 0.44$, presumably, due to a different protocol for the background removal. Either way, $\chi^{-1}(T)$ is strongly nonlinear and its slope gets smaller with the temperature. If one defines “instantaneous” CW parameters as $C(T) = 1/(d\chi^{-1}(T)/dT)$ and $\Theta(T) = T - C(T)/\chi(T)$, then $\Theta(T)$ is becoming increasingly antiferromagnetic with temperature, and $C(T)$ also grows, corresponding

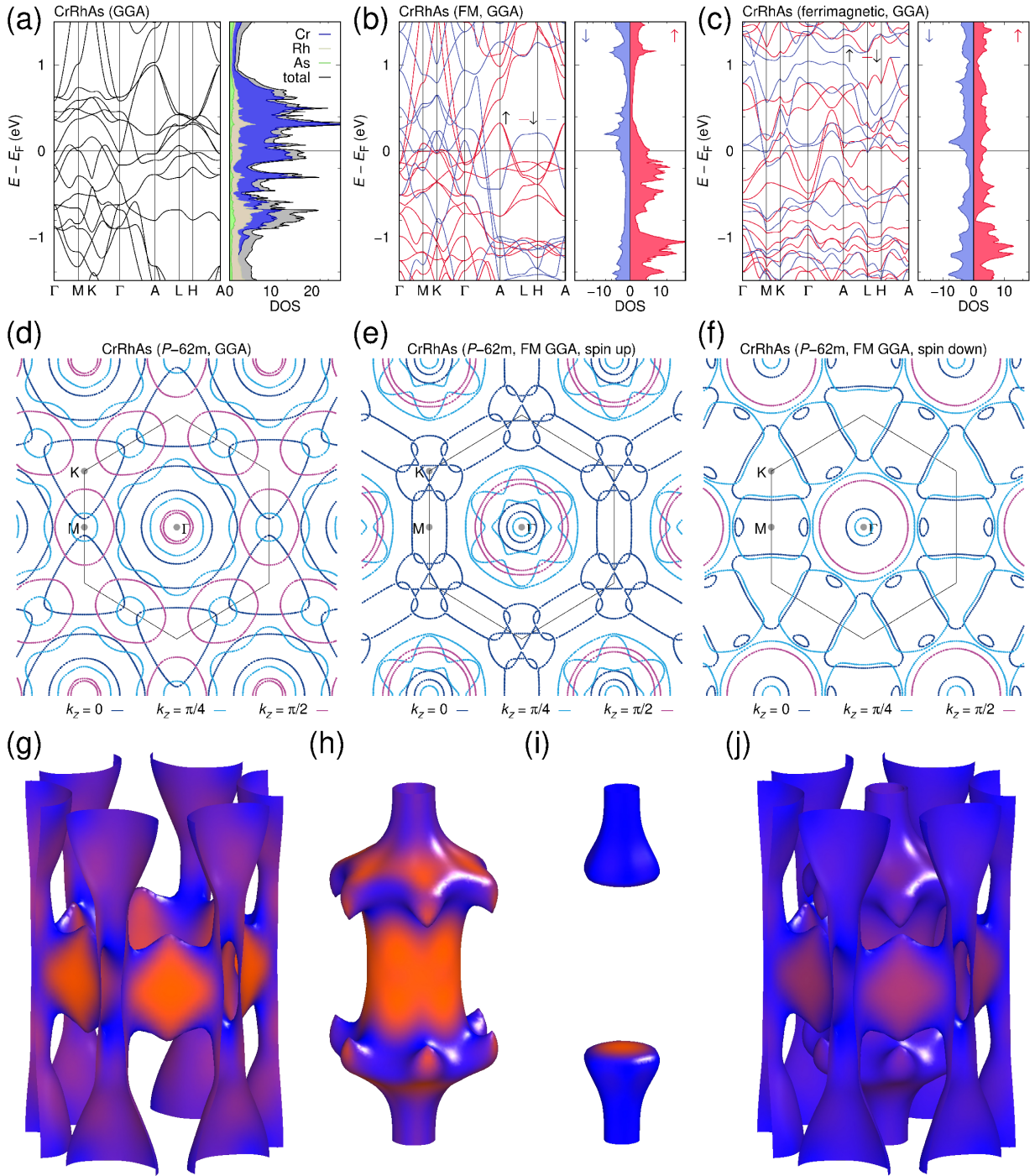


FIG. 9. GGA electronic structure of CrRhAs. (a) Non-magnetic, (b) ferromagnetic and (c) ferrimagnetic bands with corresponding densities of states. (d) $k_x - k_y$ plane cuts of the Fermi surface for three different values of k_z . (e), (f) the same for the ferromagnetic solution. (g)-(j) 3D contour plots of the non-magnetic Fermi surface; (g)-(i) are three individual FS sheets, and (j) shows all of them together. In (g)-(j), color indicates Fermi velocity where blue is low, orange high.

to increasingly large effective moments.

All these observations, as strange as they may seem on the first glance, find natural explanations in our Hamiltonian and proposed ground state. Indeed, the former is dominated by the very strong J_2 interaction, which itself corresponds to a temperature scale of $2J_2$ (2 for the

coordination number) of the order of 1000 K, or if converted to the CW temperature and assuming spin 3/2 and the quantum factor $(S + 1)/S = 5/3$, corresponds to $T_{CW} = -578$ K. This indicates that at room temperature the isolated trimers formed by the J_2 bonds are still strongly correlated, forming complexes with

strongly suppressed net magnetic moment. As a result, the true CW regime is not attained until $T \gtrsim 600$ K, and the observed behavior is nothing but a graduate crossover from the fully correlated trimers with the effective moment $m_{\text{eff}} \ll 1 \mu_B$ and T_{CW} defined by the other (besides J_2) interactions in the system (which is on the order of -72 K), and the very high temperature regime, not reached in the reported experiments, where $m_{\text{eff}} \sim \sqrt{3 \cdot 5} = 3.87 \mu_B$, and $T_{\text{CW}} \sim -650$ K. Finally, the relatively small value of T_N compared to the high T_{CW} temperature finds a natural explanation in the fact that the intra-trimer ordering that does happen at high temperature is not related to the temperature at which the individual triangles order with respect to each other; the latter is determined by the much weaker inter-trimer interactions. In fact, an upper boundary on the mean-field transition temperature can be derived by taking all interactions but J_2 with the same sign (remember that, for instance, J_1 and J_3 , albeit being of the opposite signs, cooperate in the suggested ordering). This gives an estimate for the maximally possible ordering temperature of 346 K. The experimental number is right between the lower estimate of 72 K and this upper bound.

VII. ELECTRONIC STRUCTURE OF CrRhAs

Finally, we turn our attention to the band structure and Fermi surface of CrRhAs. We use GGA calculations with the FPLO basis to determine both non-magnetic (Fig. 9(a)) and examples of magnetic band structures (Fig. 9(b)-(c)). At the Fermi level, most of the density of states derives from Cr $3d$, with only small Rh $4d$ and very small As $3p$ contributions (Fig. 9(a)). In the nonmagnetic bands, a Dirac point at the K point can be seen about 0.4 eV above the Fermi level but flat bands are hard to make out. CrRhAs remains metallic in both ferromagnetic and ferrimagnetic states (Fig. 9(b)-(c)) as well as in antiferromagnetic spin configurations (not shown). However, DOS at E_F is substantially lower in magnetic compared to nonmagnetic states. The non-magnetic Fermi surface (see Fig. 9(d) for cuts, Fig. 9(h)-(i) for 3D plots) has some cylinder-like 2D features but also significant variation along k_z . The FS for the ferromagnetic solution (Fig. 9(e)-(f)) is not much simpler.

VIII. CONCLUSIONS

We studied one member of a large family of XYZ compounds with spacegroup $P\bar{6}2m$ that contains twisted kagome and trimerized (distorted triangular) lattices. As many as 70 of them have significant magnetism on a kagome lattice, and despite the distorted geometry, the magnetic interaction Hamiltonian remains the same as ideal kagome at the nearest neighbor level, which makes this series of compounds a fertile playground for kagome physics. We used CrRhAs as an example to study different spin spiral and noncollinear energies.

To this end, we have calculated within the density functional theory the total energies of six different in-plane spin spirals, three different out-of-plane spirals, and two continuously varying non-collinear magnetic arrangements with the $\mathbf{q} = 0$ periodicity, a total of more than 230 first principle calculations. Based on these data, we generated a magnetic Hamiltonian that fits all these energies reasonably well (with max deviation within 15 meV). Interestingly, the resulting Hamiltonian was rather unusual in several aspects: first, we found that Heisenberg exchange interactions could not provide a satisfactory fit; adding ring exchange terms proved indispensable, especially for the two $\mathbf{q} = 0$ sets of calculations. Second, we found that the nearest neighbor exchange coupling was ferromagnetic, and thus not frustrated, but the leading (by far) interaction was the next nearest neighbor antiferromagnetic coupling in the twisted kagome plane, which is frustrated and leads to a curious, and, to the best of our knowledge, never discussed before magnetic Hamiltonian. The ground state of this Hamiltonian is controlled by independent triangles of a certain vector spin chirality, either positive or negative, but the same for all triangles, and varying toroidicity between these triangles. Furthermore, it has a potential to develop, either statically due to spin-orbit coupling, or dynamically through topological field fluctuations, scalar spin chirality and topological Hall effect. These possibilities, however, go beyond the scope of our paper.

We hope that this study would motivate further experimental and theoretical research into this intriguing family, and particularly this specific system.

ACKNOWLEDGMENTS

Y.N.H. is supported by the National Natural Science Foundation of China (under Grant No. 11904319), and she thanks Bao Weicheng for valuable help in this research. I.I.M. acknowledges support from the U.S. Department of Energy through the grant No. DE-SC0021089.

[1] Y. Zhou, K. Kanoda, and T.-K. Ng, Quantum spin liquid states, *Rev. Mod. Phys.* **89**, 025003 (2017).

[2] C. Broholm, R. J. Cava, S. A. Kivelson, D. G. Nocera,

- M. R. Norman, and T. Senthil, Quantum spin liquids, *Science* **367**, eaay0668 (2020).
- [3] L. Savary and L. Balents, Quantum spin liquids: A review, *Rep. Prog. Phys.* **80**, 016502 (2016).
- [4] L. Balents, Spin liquids in frustrated magnets, *Nature* **464**, 199 (2010).
- [5] M. P. Shores, E. A. Nytko, B. M. Bartlett, and D. G. Nocera, A Structurally Perfect $S = 1/2$ Kagomé Antiferromagnet, *J. Am. Chem. Soc.* **127**, 13462 (2005).
- [6] T.-H. Han, J. S. Helton, S. Chu, D. G. Nocera, J. A. Rodriguez-Rivera, C. Broholm, and Y. S. Lee, Fractionalized excitations in the spin-liquid state of a kagome-lattice antiferromagnet, *Nature* **492**, 406 (2012).
- [7] Q. Barthélemy, A. Demuer, C. Marcenat, T. Klein, B. Bernu, L. Messio, M. Velázquez, E. Kermarrec, F. Bert, and P. Mendels, Specific heat of the kagome antiferromagnet herbertsmithite in high magnetic fields, *Phys. Rev. X* **12**, 011014 (2022).
- [8] B. Fåk, E. Kermarrec, L. Messio, B. Bernu, C. Lhuillier, F. Bert, P. Mendels, B. Koteswararao, F. Bouquet, J. Ollivier, A. D. Hillier, A. Amato, R. H. Colman, and A. S. Wills, Kapellasite: A kagome quantum spin liquid with competing interactions, *Phys. Rev. Lett.* **109**, 037208 (2012).
- [9] Y. Iqbal, H. O. Jeschke, J. Reuther, R. Valentí, I. I. Mazin, M. Greiter, and R. Thomale, Paramagnetism in the kagome compounds $(\text{Zn, Mg, Cd})\text{Cu}_3(\text{OH})_6\text{Cl}_2$, *Phys. Rev. B* **92**, 220404 (2015).
- [10] Q. Barthélemy, P. Puphal, K. M. Zoch, C. Krellner, H. Luetkens, C. Baines, D. Sheptyakov, E. Kermarrec, P. Mendels, and F. Bert, Local study of the insulating quantum kagome antiferromagnets $\text{YCu}_3(\text{OH})_6\text{O}_x\text{Cl}_{3-x}$ ($x = 0, 1/3$), *Phys. Rev. Mater.* **3**, 074401 (2019).
- [11] M. Hering, F. Ferrari, A. Razpopov, I. I. Mazin, R. Valentí, H. O. Jeschke, and J. Reuther, Phase diagram of a distorted kagome antiferromagnet and application to Y-kapellasite, *npj Comput. Mater.* **8**, 10 (2022).
- [12] D. Guterding, R. Valentí, and H. O. Jeschke, Reduction of magnetic interlayer coupling in barlowite through isoelectronic substitution, *Phys. Rev. B* **94**, 125136 (2016).
- [13] Z. Feng, Z. Li, X. Meng, W. Yi, Y. Wei, J. Zhang, Y.-C. Wang, W. Jiang, Z. Liu, S. Li, F. Liu, J. Luo, S. Li, G.-Q. Zheng, Z. Y. Meng, J.-W. Mei, and Y. Shi, Gapped spin-1/2 spinon excitations in a new kagome quantum spin liquid compound $\text{Cu}_3\text{Zn}(\text{OH})_6\text{FBr}$, *Chin. Phys. Lett.* **34**, 077502 (2017).
- [14] M. Kang, L. Ye, S. Fang, J.-S. You, A. Levitan, M. Han, J. I. Facio, C. Jozwiak, A. Bostwick, E. Rotenberg, M. K. Chan, R. D. McDonald, D. Graf, K. Kaznatcheev, E. Vescovo, D. C. Bell, E. Kaxiras, J. van den Brink, M. Richter, M. Prasad Ghimire, J. G. Checkelsky, and R. Comin, Dirac Fermions and flat bands in the ideal kagome metal FeSn , *Nat. Mater.* **19**, 163 (2020).
- [15] M. Han, H. Inoue, S. Fang, C. John, L. Ye, M. K. Chan, D. Graf, T. Suzuki, M. P. Ghimire, W. J. Cho, E. Kaxiras, and J. G. Checkelsky, Evidence of two-dimensional flat band at the surface of antiferromagnetic kagome metal FeSn , *Nat. Commun.* **12**, 5345 (2021).
- [16] L. Ye, M. Kang, J. Liu, F. von Cube, C. R. Wicker, T. Suzuki, C. Jozwiak, A. Bostwick, E. Rotenberg, D. C. Bell, L. Fu, R. Comin, and J. G. Checkelsky, Massive Dirac fermions in a ferromagnetic kagome metal, *Nature* **555**, 638 (2018).
- [17] N. J. Ghimire, R. L. Dally, L. Poudel, D. C. Jones, D. Michel, N. T. Magar, M. Bleuel, M. A. McGuire, J. S. Jiang, J. F. Mitchell, J. W. Lynn, and I. I. Mazin, Competing magnetic phases and fluctuation-driven scalar spin chirality in the kagome metal YMn_6Sn_6 , *Sci. Adv.* **6**, eabe2680 (2020).
- [18] M. Li, Q. Wang, G. Wang, Z. Yuan, W. Song, R. Lou, Z. Liu, Y. Huang, Z. Liu, H. Lei, Z. Yin, and S. Wang, Dirac cone, flat band and saddle point in kagome magnet YMn_6Sn_6 , *Nat. Commun.* **12**, 3129 (2021).
- [19] H. Zhang, X. Feng, T. Heitmann, A. I. Kolesnikov, M. B. Stone, Y.-M. Lu, and X. Ke, Topological magnon bands in a room-temperature kagome magnet, *Phys. Rev. B* **101**, 100405 (2020).
- [20] X. Wu, T. Schwemmer, T. Müller, A. Consiglio, G. Sangiovanni, D. Di Sante, Y. Iqbal, W. Hanke, A. P. Schnyder, M. M. Denner, M. H. Fischer, T. Neupert, and R. Thomale, Nature of Unconventional Pairing in the Kagome Superconductors AV_3Sb_5 ($A=\text{K, Rb, Cs}$), *Phys. Rev. Lett.* **127**, 177001 (2021).
- [21] L. Nie, K. Sun, W. Ma, D. Song, L. Zheng, Z. Liang, P. Wu, F. Yu, J. Li, M. Shan, D. Zhao, S. Li, B. Kang, Z. Wu, Y. Zhou, K. Liu, Z. Xiang, J. Ying, Z. Wang, T. Wu, and X. Chen, Charge-density-wave-driven electronic nematicity in a kagome superconductor, *Nature* **604**, 59 (2022).
- [22] K. Y. Chen, N. N. Wang, Q. W. Yin, Y. H. Gu, K. Jiang, Z. J. Tu, C. S. Gong, Y. Uwatoko, J. P. Sun, H. C. Lei, J. P. Hu, and J.-G. Cheng, Double Superconducting Dome and Triple Enhancement of T_c in the Kagome Superconductor CsV_3Sb_5 under High Pressure, *Phys. Rev. Lett.* **126**, 247001 (2021).
- [23] C. Mielke, D. Das, J.-X. Yin, H. Liu, R. Gupta, Y.-X. Jiang, M. Medarde, X. Wu, H. C. Lei, J. Chang, P. Dai, Q. Si, H. Miao, R. Thomale, T. Neupert, Y. Shi, R. Khasanov, M. Z. Hasan, H. Luetkens, and Z. Guguchia, Time-reversal symmetry-breaking charge order in a kagome superconductor, *Nature* **602**, 245 (2022).
- [24] C. Lacroix, Frustrated metallic systems: A review of some peculiar behavior, *J. Phys. Soc. Jpn.* **79**, 011008 (2010).
- [25] S. A. Siddiqui, J. Sklenar, K. Kang, M. J. Gilbert, A. Schleife, N. Mason, and A. Hoffmann, Metallic antiferromagnets, *J. Appl. Phys.* **128**, 040904 (2020).
- [26] S. Ohta, T. Kanomata, and T. Kaneko, Magnetic properties of CrRhAs and CrRuAs , *J. Mag. Mag. Mater.* **90-91**, 171 (1990).
- [27] T. Kanomata, T. Kawashima, H. Utsugi, T. Goto, H. Hasegawa, and T. Kaneko, Magnetic properties of the intermetallic compounds $\text{MM}'\text{X}$ ($M=\text{Cr, Mn}$, $M'=\text{Ru, Rh, Pd}$, and $X=\text{P, As}$), *J. Appl. Phys.* **69**, 4639 (1991).
- [28] T. Kaneko, T. Kanomata, T. Kawashima, S. Mori, S. Miura, and Y. Nakagawa, High-field magnetization in intermetallic compounds $\text{MM}'\text{X}$ ($M=\text{Mn}$, Cr ; $M'=\text{Ru}$, Rh , Pd ; $X=\text{As}$, P), *Physica B* **177**, 123 (1992).
- [29] S. Ohta, T. Kaneko, H. Yoshida, T. Kanomata, and H. Yamauchi, Pressure effect on the magnetic transition temperatures and thermal expansion in chromium ternary pnictides CrMAs ($M = \text{Ni, Rh}$), *J. Mag. Mag. Mater.* **150**, 157 (1995).
- [30] K. Momma and F. Izumi, *VESTA3* for three-dimensional visualization of crystal, volumetric and morphology data, *J. Appl. Crystallogr.* **44**, 1272 (2011).

- [31] A. Jain, S. P. Ong, G. Hautier, W. Chen, W. D. Richards, S. Dacek, S. Cholia, D. Gunter, D. Skinner, G. Ceder, and K. A. Persson, Commentary: The Materials Project: A materials genome approach to accelerating materials innovation, *APL Mater.* **1**, 011002 (2013).
- [32] See Supplemental Material at [TO BE INSERTED BY THE EDITORS] for additional information on other magnetic XYZ compounds, CrRhAs neighbor information, energy expressions for spirals and additional fits of DFT energies.
- [33] G. Kresse and J. Furthmüller, Efficient iterative schemes for ab initio total-energy calculations using a plane-wave basis set, *Phys. Rev. B* **54**, 11169 (1996).
- [34] G. Kresse and J. Furthmüller, Efficiency of ab-initio total energy calculations for metals and semiconductors using a plane-wave basis set, *Comput. Mater. Sci.* **6**, 15 (1996).
- [35] G. Kresse and J. Hafner, Ab initio molecular dynamics for liquid metals, *Phys. Rev. B* **47**, 558 (1993).
- [36] K. Koepnik and H. Eschrig, Full-potential nonorthogonal local-orbital minimum-basis band-structure scheme, *Phys. Rev. B* **59**, 1743 (1999).
- [37] J. P. Perdew, K. Burke, and M. Ernzerhof, Generalized gradient approximation made simple, *Phys. Rev. Lett.* **77**, 3865 (1996).
- [38] B. Deyris, J. Roy-Montreuil, A. Michel, R. Fruchart, J. P. Senateur, and D. Boursier, Influence de l'électronegativité sur l'apparition de l'ordre dans les phases $MM'As$ ($M=Ru, Rh, Pd$; M' = element des transition $3d$), *Annales de Chimie (Paris)* **4**, 411 (1979).
- [39] L. M. Sandratskii, Symmetry analysis of electronic states for crystals with spiral magnetic order. I. General properties, *J. Phys.: Condens. Matter* **3**, 8565 (1991).

CrRhAs: a member of a large family of metallic kagome antiferromagnets – Supplemental Material –

Y. N. Huang

Department of Physics, Zhejiang University of Science and Technology, Hangzhou 310023, People's Republic of China

Harald O. Jeschke

Research Institute for Interdisciplinary Science, Okayama University, Okayama 700-8530, Japan

Igor I. Mazin*

*Department of Physics & Astronomy, George Mason University, Fairfax, VA 22030, USA and
Quantum Science and Engineering Center, George Mason University, Fairfax, VA 22030, USA.*

(Dated: November 9, 2022)

I. XYZ COMPOUNDS WITH SIGNIFICANT MAGNETISM

Initially, we classified XYZ compounds with space group $P\bar{6}2m$ (no. 189) by groups of elements. By analyzing all $P\bar{6}2m$ XYZ compounds in the Materials Project database, we found that X , Y , Z atoms belong to finite groups of elements as shown in Table S1.

With poor metal, we refer to Al, Ga, In, Sn, Tl, Pb, Bi. As metalloid, we classify B, Si, Ge, As and Sb. Relevant nonmetals are H, C, N and P. Specifically, the XY combination of element series is shown in Table S2.

TABLE S1: XYZ compounds classified by periodic table series

Atom	Element Series
X	actinide, alkaline earth metal, lanthanide, poor metal, transition metal
Y	alkali metal, alkaline earth metal, lanthanide, metalloid, poor metal, transition metal
Z	alkaline earth metal, lanthanide, metalloid, nonmetal, poor metal, transition metal

TABLE S2: XY combination of groups of elements.

X group	Y group
actinide	metalloid
actinide	poor metal
alkaline earth metal	alkali metal
alkaline earth metal	poor metal
alkaline earth metal	transition metal
lanthanide	alkali metal
lanthanide	alkaline earth metal
lanthanide	metalloid
lanthanide	poor metal
lanthanide	transition metal
poor metal	lanthanide
poor metal	transition metal
transition metal	alkali metal
transition metal	alkaline earth metal
transition metal	metalloid
transition metal	poor metal
transition metal	transition metal

We choose $P\bar{6}2m$ XYZ compounds with significant magnetism from the Materials Project (MP)[S1], and organize them into Table S3. mp-id is the material ID of MP. X is the kagome atom, Y is trimer atom. $|v|(X)$ and $|v|(Y)$ are

* imazin2@gmu.edu

the v values of X and Y respectively where $v = x - 1/2$ is determined from the fractional coordinate x of the X or Y atom (see also main text). The ICSD column shows whether the compound exists and has been reported to the Inorganic Crystal Structure Database (ICSD).

TABLE S3: XYZ (space group $P\bar{6}2m$) compounds with significant magnetism.

mp-id	compound	X	$ v (X)$	Y	$ v (Y) $	ICSD
mp-20665	CeInCu	Ce	0.081851	In	0.252775	yes
mp-15683	CrRhAs	Cr	0.092491	Rh	0.245181	yes
mp-1205827	CrPdAs	Cr	0.103397	Pd	0.232872	no
mp-1087537	CrPdP	Cr	0.105917	Pd	0.231023	yes
mp-4989	CrNiAs	Cr	0.095091	Ni	0.244877	yes
mp-1206397	CrCoAs	Cr	0.086577	Co	0.252504	no
mp-1206083	CrFeAs	Cr	0.087428	Fe	0.253454	no
mp-1079966	CrNiP	Cr	0.091987	Ni	0.244212	yes
mp-1091389	EuInPd	Eu	0.089105	In	0.252248	yes
mp-1225012	FeRhAs	Fe	0.103656	Rh	0.236774	no
mp-1224852	FeRhP	Fe	0.110326	Rh	0.231339	no
mp-1080653	FeNiP	Fe	0.098632	Ni	0.242936	yes
mp-1080612	GdAlCu	Gd	0.085396	Al	0.267555	yes
mp-20332	GdMgPd	Gd	0.086926	Mg	0.257178	yes
mp-22028	GdMgPt	Gd	0.090582	Mg	0.25546	yes
mp-623988	GdCdPd	Gd	0.093488	Cd	0.245842	yes
mp-20224	GdInPd	Gd	0.090917	In	0.242642	yes
mp-1101090	GdAlNi	Gd	0.080304	Al	0.267974	yes
mp-1080178	GdZnPd	Gd	0.096443	Zn	0.249717	yes
mp-30692	GdTlPd	Gd	0.09759	Tl	0.234001	yes
mp-574004	GdMgGa	Gd	0.075155	Mg	0.256293	yes
mp-20058	GdAlPd	Gd	0.082467	Al	0.265203	yes
mp-1101056	GdMgIn	Gd	0.065156	Mg	0.259364	yes
mp-1079690	GdAgSi	Gd	0.083068	Ag	0.249535	yes
mp-1080496	GdInAu	Gd	0.091863	In	0.242823	yes
mp-1079739	GdSnPt	Gd	0.089816	Sn	0.244624	yes
mp-9341	GdAgGe	Gd	0.084516	Ag	0.249724	yes
mp-19745	GdInIr	Gd	0.092568	In	0.245165	yes
mp-623043	GdInRh	Gd	0.091525	In	0.245585	yes
mp-1206951	GdMgTl	Gd	0.070661	Mg	0.256942	no
mp-14210	GdLiGe	Gd	0.077382	Li	0.267255	no
mp-582029	GdInPt	Gd	0.092445	In	0.249518	yes
mp-580154	GdMgAu	Gd	0.08771	Mg	0.254229	yes
mp-21458	GdCdCu	Gd	0.088142	Cd	0.250108	yes
mp-1079035	MnPdAs	Mn	0.092059	Pd	0.238231	yes
mp-1079184	MnRhGe	Mn	0.0912	Rh	0.241729	yes
mp-10049	MnRuAs	Mn	0.095843	Ru	0.242341	yes
mp-1206331	MnPdP	Mn	0.095237	Pd	0.235672	no
mp-610972	MnPdGe	Mn	0.096695	Pd	0.235066	yes
mp-567856	MnRhAs	Mn	0.095212	Rh	0.236511	yes
mp-1079845	MnNiAs	Mn	0.085264	Ni	0.248649	yes
mp-1079806	MnTiAs	Mn	0.109278	Ti	0.238304	yes
mp-1079405	MnRhP	Mn	0.10521	Rh	0.235009	yes
mp-4238	MnFeAs	Mn	0.094506	Fe	0.245038	yes
mp-975423	MnNiP	Mn	0.100394	Ni	0.24237	yes
mp-20314	NpSnIr	Np	0.085981	Sn	0.245747	yes
mp-1091393	PuGaNi	Pu	0.082098	Ga	0.260442	yes
mp-1078774	PuGaRh	Pu	0.086028	Ga	0.252119	yes
mp-1079793	PuAlCo	Pu	0.071542	Al	0.262264	yes
mp-1080562	USnPt	U	0.087948	Sn	0.245606	yes
mp-1078683	UInPd	U	0.080172	In	0.251386	yes
mp-1078582	UInPt	U	0.08236	In	0.249319	yes
mp-1080442	UGaPd	U	0.073034	Ga	0.261463	yes
mp-1079696	USnRh	U	0.081128	Sn	0.248363	yes
mp-1080803	USnIr	U	0.083744	Sn	0.247099	yes
mp-1095127	USbRu	U	0.086204	Sb	0.242608	yes

TABLE S3: XYZ (space group $P\bar{6}2m$) compounds with significant magnetism.

mp-1091404	UInRh	U	0.081975	In	0.253257	yes
mp-21494	USnCo	U	0.081587	Sn	0.249041	yes
mp-1080077	UGaPt	U	0.078517	Ga	0.256914	yes
mp-1079949	UAlPt	U	0.074677	Al	0.262571	yes
mp-5015	UAlRh	U	0.074114	Al	0.265481	yes
mp-1078870	UGaRh	U	0.078603	Ga	0.260529	yes
mp-1079086	UAlNi	U	0.071447	Al	0.264623	yes
mp-21320	UGaNi	U	0.071759	Ga	0.261885	yes
mp-1079219	UAlIr	U	0.07841	Al	0.263225	yes
mp-1080013	UAlRu	U	0.074845	Al	0.266171	yes
mp-1078880	UGaRu	U	0.076241	Ga	0.262093	yes
mp-19811	USnRu	U	0.083475	Sn	0.248264	yes
mp-1078586	UGaCo	U	0.0795095	Ga	0.2635175	yes

II. NEAREST NEIGHBOR INFORMATION OF CRRHAS

We summarize the nearest neighbor information to a reference Cr1 atom of CrRhAs in Table S4. The in-plane distance is the projected bond length in the xy plane. n_{bonds} is the number of bonds that satisfy the in-plane distance constraint. $d_z = 0 \text{ \AA}$, $d_z = 3.718 \text{ \AA}$, $d_z = 7.436 \text{ \AA}$, $d_z = 11.154 \text{ \AA}$ correspond to successive Cr plane distances along the z direction, and J_i in each column is the hopping from the reference Cr1 atom to the corresponding Cr plane.

TABLE S4. Nearest neighbor information of CrRhAs. d_z are distances between Cr planes along z direction. Distance $d_{\text{Cr-Cr}}$ is given in brackets for easy identification of the bond. In the naming scheme of the main paper, the first column of couplings is called J_0, J_1, J_2, \dots , the second column is called J'_0, J'_1, J'_2, \dots , the third $J''_0, J''_1, J''_2, \dots$, and so on.

$d_{\text{inplane}} (\text{\AA})$	Cr1 bond to	n_{bonds}	$d_z = 0 \text{ \AA}$	$d_z = 3.718 \text{ \AA}$	$d_z = 7.436 \text{ \AA}$	$d_z = 11.154 \text{ \AA}$
0.	{Cr1}	1	J0 (0 \AA)	J2 (3.718 \AA)	J9 (7.436 \AA)	J25 (11.154 \AA)
3.384	{Cr3,Cr2}	4	J1 (3.384 \AA)	J4 (5.028 \AA)	J12 (8.170 \AA)	J26 (11.656 \AA)
4.404	{Cr3,Cr2}	2	J3 (4.404 \AA)	J5 (5.764 \AA)	J14 (8.642 \AA)	J29 (11.992 \AA)
6.384	{Cr1}	6	J6 (6.384 \AA)	J8 (7.388 \AA)	J17 (9.800 \AA)	J34 (12.852 \AA)
6.653	{Cr2,Cr3}	2	J7 (6.653 \AA)	J10 (7.622 \AA)	J19 (9.978 \AA)	J35 (12.988 \AA)
7.756	{Cr3,Cr2}	4	J11 (7.756 \AA)	J13 (8.601 \AA)	J22 (10.745 \AA)	J40 (13.585 \AA)
9.221	{Cr3,Cr2}	4	J15 (9.221 \AA)	J18 (9.942 \AA)	J28 (11.846 \AA)	J45 (14.472 \AA)
9.642	{Cr3,Cr2}	4	J16 (9.642 \AA)	J20 (10.334 \AA)	J30 (12.176 \AA)	J47 (14.744 \AA)
10.433	{Cr3,Cr2}	4	J21 (10.433 \AA)	J24 (11.076 \AA)	J33 (12.812 \AA)	J52 (15.273 \AA)
11.057	{Cr1}	6	J23 (11.057 \AA)	J27 (11.666 \AA)	J38 (13.325 \AA)	J58 (15.706 \AA)
12.593	{Cr2,Cr3}	4	J31 (12.593 \AA)	J36 (13.131 \AA)	J46 (14.625 \AA)	J68 (16.823 \AA)
12.768	{Cr1}	6	J32 (12.768 \AA)	J37 (13.298 \AA)	J48 (14.776 \AA)	J70 (16.954 \AA)

III. HAMILTONIAN COEFFICIENT EXPRESSIONS FOR $(q_x, 0, q_z)$ SPIRALS

We derived coefficient expressions C_i, C'_i, C''_i, \dots and D, D', D'' for Eq. (4) in the main text.

TABLE S5. Coefficient expression of C_i and D for $(q_x, 0, q_z)$ spin spirals.

E_0	1
C_1	$\cos(\theta_x - \phi(1) + \phi(2)) + \cos(\theta_x + \phi(2) - \phi(3)) + \cos(\phi(1) - \phi(2)) + 2 \cos(\phi(1) - \phi(3)) + \cos(\phi(2) - \phi(3))$
C_2	$\cos(\theta_x - \phi(1) + \phi(2)) + \cos(\theta_x - \phi(1) + \phi(3)) + \cos(\phi(2) - \phi(3))$
C_3	$3(2 \cos(\theta_x) + 1)$
C_4	$\cos(\theta_x + \phi(1) - \phi(3)) + \cos(\theta_x + \phi(2) - \phi(3)) + \cos(\phi(1) - \phi(2))$
C'_0	$3 \cos(\theta_z)$
C'_1	$2 \cos(\theta_z)(\cos(\theta_x - \phi(1) + \phi(2)) + \cos(\theta_x + \phi(2) - \phi(3)) + \cos(\phi(1) - \phi(2)) + 2 \cos(\phi(1) - \phi(3)) + \cos(\phi(2) - \phi(3)))$
C'_2	$2 \cos(\theta_z)(\cos(\theta_x - \phi(1) + \phi(2)) + \cos(\theta_x - \phi(1) + \phi(3)) + \cos(\phi(2) - \phi(3)))$
C'_3	$6(2 \cos(\theta_x) + 1) \cos(\theta_z)$
C'_4	$2 \cos(\theta_z)(\cos(\theta_x + \phi(1) - \phi(3)) + \cos(\theta_x + \phi(2) - \phi(3)) + \cos(\phi(1) - \phi(2)))$
C''_0	$3 \cos(2\theta_z)$
C''_1	$2 \cos(2\theta_z)(\cos(\theta_x - \phi(1) + \phi(2)) + \cos(\theta_x + \phi(2) - \phi(3)) + \cos(\phi(1) - \phi(2)) + 2 \cos(\phi(1) - \phi(3)) + \cos(\phi(2) - \phi(3)))$
C''_2	$2 \cos(2\theta_z)(\cos(\theta_x - \phi(1) + \phi(2)) + \cos(\theta_x - \phi(1) + \phi(3)) + \cos(\phi(2) - \phi(3)))$
C''_3	$6(2 \cos(\theta_x) + 1) \cos(2\theta_z)$
C''_4	$2 \cos(2\theta_z)(\cos(\theta_x + \phi(1) - \phi(3)) + \cos(\theta_x + \phi(2) - \phi(3)) + \cos(\phi(1) - \phi(2)))$
D_1	$\cos(\phi(1) - \phi(3)) \cos(\theta_x - \phi(1) + \phi(2)) + \cos(\phi(1) - \phi(3))(\cos(\theta_x + \phi(2) - \phi(3)) + \cos(\phi(2) - \phi(3)) + 1) + \cos(\theta_x) \cos(\theta_x - \phi(1) + 2\phi(2) - \phi(3)) + \cos(\phi(1) - \phi(2)) \cos(\phi(1) - \phi(3))$
D_2	$\frac{1}{2}(\cos(\phi(2) - \phi(3))(2 \cos(\theta_x - \phi(1) + \phi(2)) + 2 \cos(\theta_x - \phi(1) + \phi(3)) + 1) + \cos(2\theta_x - 2\phi(1) + \phi(2) + \phi(3)))$

The definition of $\phi(1), \phi(2), \phi(3)$ and θ_x is illustrated in Fig. S1. For θ_z , it is a common rotation angle between current plane and the next plane of all moments.

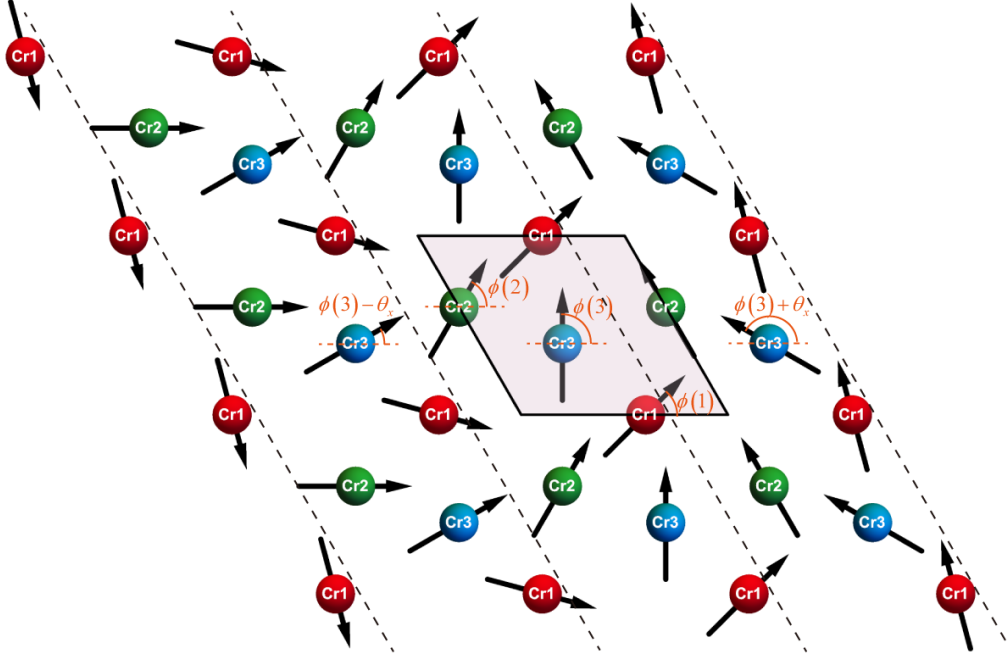


FIG. S1. An illustration of a $(q_x, 0, 0)$ spiral. $\phi(1), \phi(2), \phi(3)$ are the polar angles of Cr1, Cr2 and Cr3 moments. θ_x is the spiral angle going from one strip marked by dashed lines to the next one.

IV. ADDITIONAL ATTEMPTS OF FITTING DFT TOTAL ENERGIES

Figure S2 shows a simple $\cos(\alpha)$ fit of the noncollinear periodic calculations (the $++\alpha$ and $+-\alpha$ series). The deviations of the fit indicate that higher harmonics are necessary for a good fit, *i.e.* a pure Heisenberg Hamiltonian cannot completely represent the noncollinear DFT energies.

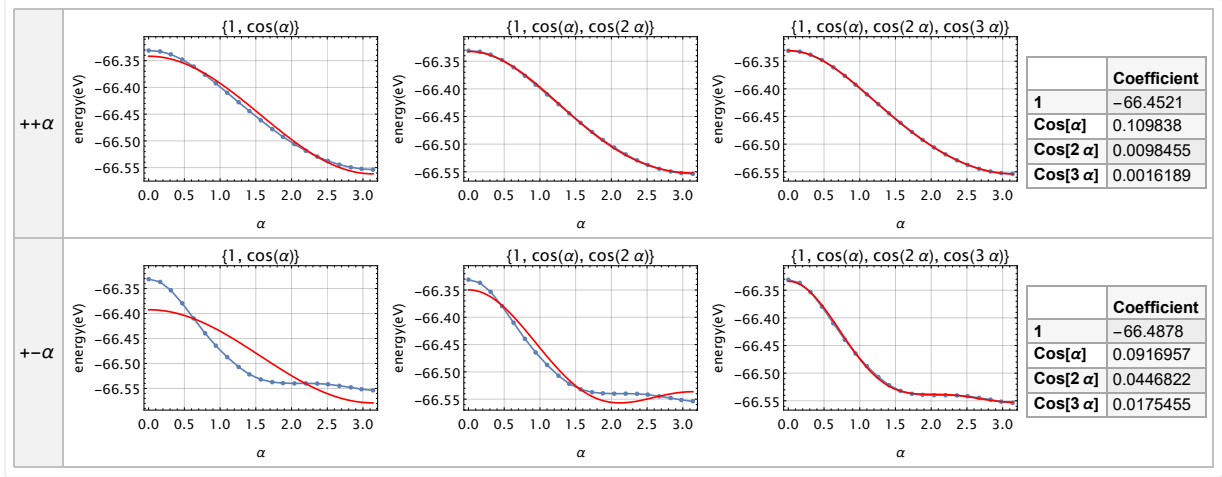


FIG. S2. Pure cosine fitting for $++\alpha$ and $+-\alpha$ series

In Figure S3, we show a fit of all spiral energies with Heisenberg exchange but without ring exchange terms. The quality of fit is clearly lower than the full fit shown in Fig. 6 of the main text, especially at $\theta = 0$ for $(120)[q00]$ and $(120)[00q]$.

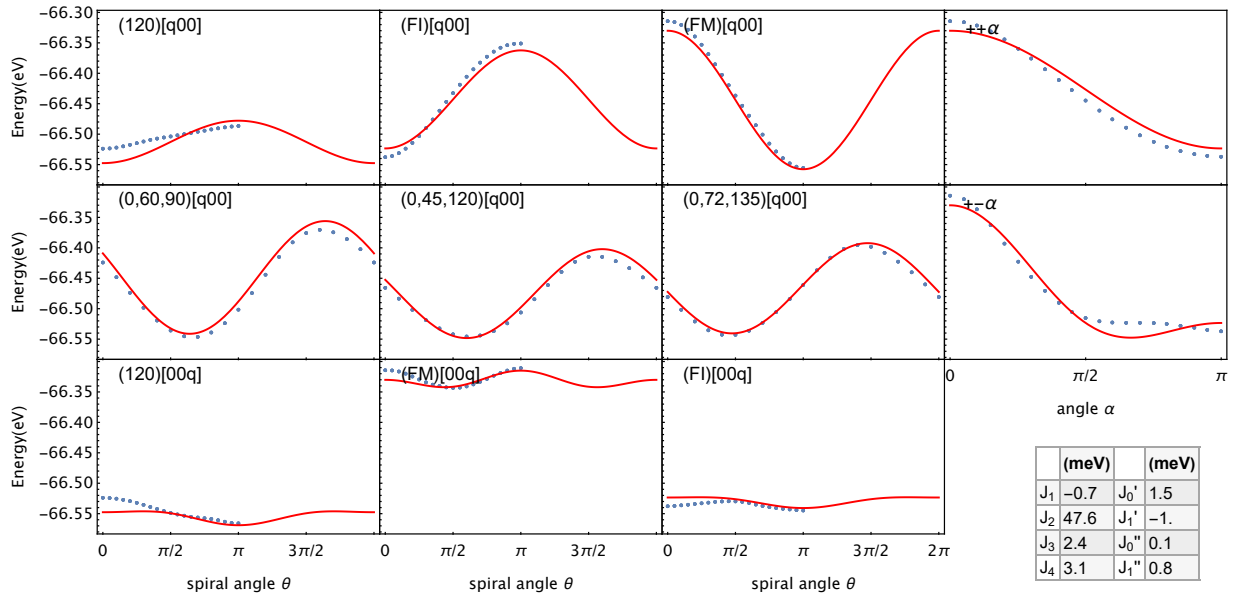


FIG. S3. Fitting all spiral energy curves without ring exchange

[S1] A. Jain, S. P. Ong, G. Hautier, W. Chen, W. D. Richards, S. Dacek, S. Cholia, D. Gunter, D. Skinner, G. Ceder, and K. A. Persson, Commentary: The Materials Project: A materials genome approach to accelerating materials innovation, APL Mater. **1**, 011002 (2013).